Journal of Sound and Vibration 329 (2010) 3247–3265

Contents lists available at ScienceDirect

Journal of Sound and Vibration

journal homepage: www.elsevier.com/locate/jsvi

Active vibration suppression of multilayered plates integrated with piezoelectric fiber reinforced composites using an efficient finite element model

S. Kapuria *, M.Y. Yasin

Department of Applied Mechanics, Indian Institute of Technology Delhi, Hauz Khas, New Delhi 110016, India

ARTICLE INFO

Article history:
Received 19 November 2009
Received in revised form
12 February 2010
Accepted 15 February 2010
Handling Editor: L.G. Tham
Available online 21 March 2010

ABSTRACT

The active vibration suppression of hybrid composite and fiber metal laminate (FML) plates integrated with piezoelectric fiber reinforced composite (PFRC) sensors and actuators is studied for the first time, using an efficient and advanced layerwise plate theory. Unlike the conventional finite elements, the equipotential condition of electroded surfaces of sensors is satisfied exactly and conveniently using a novel concept of electric node. The effective electromechanical properties of the PFRC laminas are computed using a coupled three-dimensional iso-field micromechanical model. Numerical results are presented for both classical constant gain velocity feedback (CGVF) and optimal control strategies. The instability phenomena in CGVF control with conventionally collocated actuator–sensor pairs, and its remedy with a truly collocated arrangement are illustrated. The effect of segmentation of electrodes on the control response is studied. The segmentation of electrodes leads to a multi-input–multi-output (MIMO) configuration. The effects of piezoelectric fiber orientation, volume fraction and dielectric ratio of PFRC on the control response and the actuation/sensing authority are investigated for cantilever and simply supported plates.

1. Introduction

Piezoelectrics have emerged as the most widely used materials for distributed sensors and actuators in smart structures for active vibration, shape, stability and noise control applications [1]. The advantages of piezoelectric materials over other smart materials are their easy commercial availability, efficient conversion between electrical and mechanical energy, relatively linear mechanical and electromechanical behavior (at low fields), large useful bandwidth and ease of integration into laminated composite structures. However, for large scale structural control applications such as in aerospace and automotive structures, monolithic piezoelectric actuators and sensors suffer from certain shortcomings with regard to tailorable directional actuation, robustness against damage during use and handling, ability to cover the entire structure for distributed sensing and actuation, and conformability to curved shell-type structural members. Recent developments of piezoelectric fiber reinforced composite (PFRC) materials with high strength, toughness, operating range (-1500 to 2800 V), life (200 million cycles) and conformability to curved surfaces have addressed these concerns [2]. Fiber metal laminate (FML) consisting of alternating layers of thin metallic sheets and fiber prepregs (aramid, carbon, glass, etc.) is fast emerging as a new structural material for aerospace and automobile applications in view of its higher specific strength,

* Corresponding author. Tel.: +91 11 26591218; fax: +91 11 26581119.
E-mail addresses: kapuria@am.iitd.ac.in (S. Kapuria), yaqoob.yasin@rediffmail.com (M.Y. Yasin).

0022-460X/$ - see front matter © 2010 Elsevier Ltd. All rights reserved.
doi:10.1016/j.jsv.2010.02.019

good plasticity, impact resistance, processability, light weight and excellent fatigue properties [3]. The present work deals with the active vibration control of hybrid composite and FML plate structures integrated with monolithic piezoelectric as well as PFRC sensors and actuators using an advanced computationally efficient mechanics model.

Analysis and design of smart laminated plate/shell-like structures integrated with distributed piezoelectric sensors and actuators for active vibration control require a computationally efficient and accurate model for the mechanics of the hybrid laminate, its efficient numerical implementation for structures and components of arbitrary shape and geometry, a suitable control theory and appropriate hardware. Most studies on active vibration control hybrid plate-type structures have been carried out using equivalent single layer (ESL) theories such as the classical theory (CLT), first order shear deformation theory (FSDT) and third order theory (TOT). These theories assume a global polynomial distribution of the displacement variables along the thickness direction across all layers, independent of the lay-up and material properties of the layers, and differ from each other by the degree of the polynomial. Uncoupled CLT [4–6], and FSDT [7] have been employed for active vibration control studies on hybrid laminated plates, which include the stiffness of the piezoelectric layers, but do not consider the electric potentials as independent variables (i.e. neglects the two-way electromechanical coupling). The neglect of full electromechanical coupling in uncoupled theories may cause significant inaccuracy in the predicted response, particularly for the sensory electric potential whose accuracy is crucial for the closed loop control. Finite element (FE) models have been developed incorporating the electric potential DOF based on the coupled CLT [8–10], FSDT [11–15] and TOT [16], for closed loop vibration control of hybrid plates. The ESL theories are computationally very efficient as the number of primary displacement variables is independent of the number of layers, but they are often inadequate for predicting accurate response of such hybrid laminated structures having strong electromechanical inhomogeneities across the thickness. Few studies have been reported using 3D solid elements [17,18] and layerwise theories (LWTs) [19], which are accurate, but the number of DOF increases proportionally with the number of layers.

In conventional finite elements, the electric DOF are treated as nodal variables [13–16] or elemental variables [9,12]. In such cases, the output signal from the electroded sensor surface is to be computed by averaging the electric DOF of nodes/elements covering the surface, which is an approximate and cumbersome process in the context of FE. In most cases, this is not followed and the equipotential condition is violated, making the control results unrealistic.

The performance of an active vibration suppression system strongly depends on the control algorithm. Most vibration control studies on smart plates employ constant gain velocity feedback (CGVF) control [6,8,9,12,13,16] and linear quadratic regulator (LQR) control [5,7,10,14,17,19]. In the CGVF control strategy, the stability of the system is guaranteed only when the actuators and sensors are truly collocated. The LQR algorithm does not require collocated actuator–sensor pairs for stability, but it requires the measurement of all state variables, which is a difficult proposition. The linear quadratic Gaussian (LQG) controller circumvents this difficulty, by employing an optimal observer for estimating the state variables from the measured outputs (sensory voltage in the present case). This controller, which is more realistic, has been applied to control of smart plates in very few studies, e.g. by Dong et al. [18] and Kumar et al. [15].

No study has been reported so far on the optimal vibration control of hybrid plates integrated with PFRC sensors and actuators. This work presents a study on the active vibration control of smart laminated plates equipped with electroded monolithic piezoelectric and PFRC sensors and actuators, using a FE based on the fully coupled efficient layerwise theory presented recently by Kapuria and Kulkarni [20]. The theory retains the accuracy of LWTs and economy of ESL theories. The inplane displacements are initially assumed to follow a layerwise linear variation with a global cubic variation in the thickness direction, but the number of primary variables is subsequently reduced to only five (as in the TOT), by imposing the conditions of continuity of transverse shear stresses at the layer interfaces and shear tractions on the top and bottom surfaces. The electric potential is assumed to follow a quadratic variation across the piezoelectric layers. Unlike in the existing FEs, the equipotential condition of the electroded surface of piezoelectric sensors is enforced accurately and conveniently by attaching the electric DOF corresponding to the electroded surface to a separate electric node that has no physical coordinates. The effective electromechanical properties of the PFRC laminas are computed using a coupled 3D iso-field micromechanical model. A reduced-order state space model is used for designing the control system. Numerical results are presented for hybrid angle–ply composite and FML plates, using both classical (CGVF) and optimal control strategies (LQR and LQG). Case studies on CGVF control are performed to show the instability phenomena in closed-loop response with conventionally collocated actuator–sensor pairs, and a truly collocated arrangement to remove the instability is illustrated. The effect of segmentation of electrodes on the control response is studied. The segmentation of electrodes leads to a multi-input–multi-output (MIMO) configuration. The effects of piezoelectric fiber orientation, volume fraction and dielectric ratio of PFRC on the control response and the actuation/sensing authority are investigated for cantilever and simply supported plates.

2. Modeling of the piezolaminated plate

2.1. Micromechanics of PFRC

For the PFRC materials used in laminated structures, the piezoelectric fibers are oriented in the plane of structures, while the poling and the electric field are along the thickness direction, i.e. perpendicular to the fiber (Fig. 1). Bent [21] presented a micromechanics model based on the coupled iso-field method to predict the effective electromechanical properties of such PFRC

laminas, considering the uniaxial stress fields [22]. This method was extended to the 3D case by Kapuria and Kumari [23]. In this method, the effective properties are obtained for representative volume element (RVE) of two possible connectivities for the piezoelectric fiber and matrix phases: models A and B with material connectivity on x_1–x_2 and x_1–x_3 planes, respectively, as shown in Fig. 2. The strain and the electric field components parallel to the connecting plane of two phases are assumed to be uniform and the same in both phases (iso-field condition), and iso-stress and iso-electric displacement conditions are assumed to exist along normal to the connecting plane. For the case of combined model (AB), the material properties of piezoelectric fiber phase in model B are replaced with the effective properties from model A.

2.2. Efficient layerwise theory

The fully coupled efficient layerwise (zigzag) theory presented by Kapuria and Kulkarni [20] is extended to PFRC materials for the present study. Consider a hybrid angle–ply composite plate (Fig. 3) with some piezoelectric sensor/

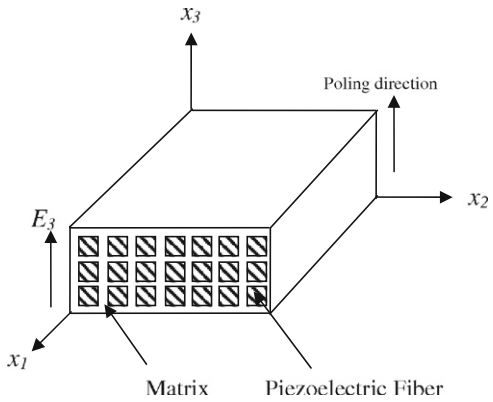

Fig. 1. Schematic representation of PFRC.

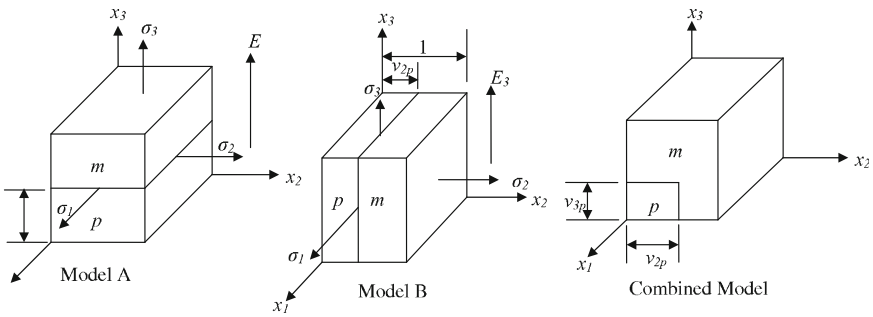

Fig. 2. Representative volume elements for iso-field model (p-piezoceramic, m-matrix).

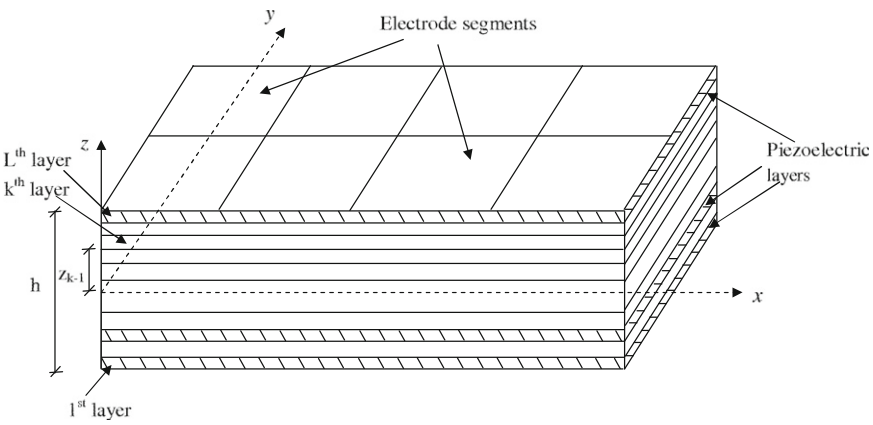

Fig. 3. Geometry of a hybrid plate.

actuator layers with poling along the thickness direction z. The piezoelectric layers may be of monolithic piezoelectric materials with class mm2 symmetry or made up of PFRC materials with unidirectional piezoelectric fibers at any arbitrary angle α^k to the x-axis. The effective electromechanical properties of the PFRC laminas are computed using the micromechanics model described in the preceding section. The piezoelectric layers are electroded at the surfaces in segments, where equipotential condition exists. The electric potential ϕ is assumed to follow a quadratic variation across the piezoelectric layers. While the electric potential at the surface will be constant over electroded segment, within the layer, it will vary in inplane directions (x,y) due to the direct piezoelectric effect. To be able to implement this differential interpolation in the FE, the piecewise quadratic variation of ϕ is described in terms of surface potentials ϕ^j at $z=z_\phi^j$ and internal quadratic component ϕ_c^l at $z=(z_\phi^l+z_\phi^{l+1})/2$:

$$\phi(x,y,z,t)=\Psi_\phi^j(z)\phi^j(x,y,t)+\Psi_c^l(z)\phi_c^l(x,y,t), \tag{1}$$

where $j=1,2,\ldots,n_\phi$ and $l=1,2,\ldots,n_\phi-1$, and the summation convention is used for repeated indices j and l. $\Psi_\phi^j(z)$ and $\Psi_c^l(z)$ are the piecewise linear and quadratic functions, respectively, given by

$$\Psi_\phi^j(z)=\left\{\begin{array}{ll} 0 & \text{if } \le z_\phi^{j-1} \quad \text{or if } z\ge z_\phi^{j+1} \\ (z-z_\phi^{j-1})/(z_\phi^j-z_\phi^{j-1}) & \text{if } z_\phi^{j-1}<z<z_\phi^j \\ (z_\phi^{j+1}-z)/(z_\phi^{j+1}-z_\phi^j) & \text{if } z_\phi^j<z<z_\phi^{j+1} \end{array}\right\},$$

$$\Psi_c^l(z)=\left\{\begin{array}{ll} 4(z_\phi^{l+1}-z)(z-z_\phi^l)/(z_\phi^{l+1}-z_\phi^l)^2 & \text{if } z_\phi^l\le z\le z_\phi^{l+1} \\ 0 & \text{otherwise} \end{array}\right\}. \tag{2}$$

The transverse displacement w is approximated by accounting for the transverse normal strain due to electric field. Thus integrating $\varepsilon_z=w_{,z}\simeq-\overline{d}_{33}\phi_{,z}$ yields

$$w(x,y,z,t)=w_0(x,y,t)-\{\overline{\Psi}_\phi^j(z)\phi^j(x,y,t)+\overline{\Psi}_c^l(z)\phi_c^l(x,y,t)\}, \tag{3}$$

where $\overline{\Psi}_\phi^j(z)=\int_0^z\overline{d}_{33}\Psi_{\phi,z}^j(z)\,dz$, $\overline{\Psi}_c^l=\int_0^z\overline{d}_{33}\Psi_{c,z}^l(z)\,dz$, d_{ij} denotes the piezoelectric strain constants and the overbar signifies reduced property due to the usual zero transverse normal stress ($\sigma_z\simeq0$) assumption.

The inplane displacements u_x,u_y (for the k th layer) are assumed to follow a global third order variation in z, combined with a layerwise linear variation:

$$\mathbf{u}(x,y,z,t)=\mathbf{u}_k(x,y,t)-z\mathbf{w}_{0_d}(x,y,t)+z\boldsymbol{\psi}_k(x,y,t)+z^2\boldsymbol{\xi}(x,y,t)+z^3\boldsymbol{\eta}(x,y,t), \tag{4}$$

where

$$\mathbf{u}=\begin{bmatrix}u_x\\u_y\end{bmatrix},\quad \mathbf{w}_{0_d}=\begin{bmatrix}w_{0,x}\\w_{0,y}\end{bmatrix},\quad \mathbf{u}_k=\begin{bmatrix}u_{k_x}\\u_{k_y}\end{bmatrix},\quad \boldsymbol{\psi}_k=\begin{bmatrix}\psi_{k_x}\\\psi_{k_y}\end{bmatrix},\quad \boldsymbol{\xi}=\begin{bmatrix}\xi_x\\\xi_y\end{bmatrix},\quad \boldsymbol{\eta}=\begin{bmatrix}\eta_x\\\eta_y\end{bmatrix}, \tag{5}$$

$\mathbf{u}_k$ denotes the translation components of the k th layer and $\boldsymbol{\psi}_k$ is related to its shear rotations. $\boldsymbol{\xi}$ and $\boldsymbol{\eta}$ are the global quadratic and cubic terms in z. Thus, $\mathbf{u}_k$ and $\boldsymbol{\psi}_k$ represent the layerwise linear component of the assumed displacement field and the remaining terms in Eq. (4) represent the global third order variation. By imposing the conditions of continuity of transverse shear stresses $\boldsymbol{\tau}(=[\tau_{zx}\ \ \tau_{zy}]^{\mathrm{T}})$ and inplane displacements $\mathbf{u}$ at the layer interfaces and of zero shear tractions ($\boldsymbol{\tau}=\mathbf{0}$) at the top and bottom surfaces, the unknowns $\mathbf{u}_k,\boldsymbol{\psi}_k,\boldsymbol{\xi}$ and $\boldsymbol{\eta}$ for the L-layered laminate are expressed in terms of only five variables $\mathbf{u}_0$, $\boldsymbol{\psi}_0$ and w_0

$$\mathbf{u}(x,y,z,t)=\mathbf{u}_0(x,y,t)-z\mathbf{w}_{0_d}(x,y,t)+\mathbf{R}^k(z)\boldsymbol{\psi}_0(x,y,t), \tag{6}$$

where u_0 and ψ_0 correspond to the k_0th layer through which the mid-plane passes or is at the bottom of. $\mathbf{R}^k(z)$ is a 2×2 matrix of layerwise functions of z of the form

$$\mathbf{R}^k(z)=\hat{\mathbf{R}}_1^k+z\hat{\mathbf{R}}_2^k+z^2\hat{\mathbf{R}}_3+z^3\hat{\mathbf{R}}_4, \tag{7}$$

where $\hat{\mathbf{R}}_1^k,\hat{\mathbf{R}}_2^k,\hat{\mathbf{R}}_3$ and $\hat{\mathbf{R}}_4$ are 2×2 coefficient matrices which depend on the material properties and the lay-ups. Their expressions are available in [24].

2.3. Finite element formulation

The weak variational form of the 2D theory is obtained using the extended Hamilton's principle for a piezoelectric medium [25], which can be expressed, using the notation $\langle\cdots\rangle=\sum_{k=1}^{L}\int_{z_{k-1}}^{z_k}(\cdots)\,dz$ for integration across the thickness, as

$$\int_A[\langle\rho^k(\delta\mathbf{u}^{\mathrm{T}}\ddot{\mathbf{u}}+\ddot{w}\delta w)+\delta\boldsymbol{\varepsilon}^{\mathrm{T}}\boldsymbol{\sigma}+\delta\boldsymbol{\gamma}^{\mathrm{T}}\boldsymbol{\tau}-\delta\mathbf{E}^{\mathrm{T}}\mathbf{D}-D_z\delta E_z\rangle-p_z^1\delta w(x,y,z_0,t)-p_z^2\delta w(x,y,z_L,t)+D_z(x,y,z_0,t)\delta\phi^1$$
$$-D_z(x,y,z_L,t)\delta\phi^{n_\phi}]\,dA-\int_{\Gamma_L}\langle\sigma_n\delta u_n+\tau_{ns}\delta u_s+\tau_{nz}\delta w+D_n\delta\phi\rangle\,ds=0 \tag{8}$$

$\forall\ \delta u_0, \delta w_0, \delta\psi_0, \delta\phi_c^l$, and $\delta\phi^j$, where A denotes the mid-plane surface area of the plate and Γ_L is the boundary curve of the midplane of the plate with normal n and tangent s. $\boldsymbol{\sigma}, \boldsymbol{\varepsilon}, \boldsymbol{\tau}$ and $\boldsymbol{\gamma}$ denote the inplane stress, inplane strain, transverse shear stress and transverse shear strain components, respectively, and $\mathbf{E}$ and $\mathbf{D}$ denote the inplane electric field and electric displacement components, respectively, which are given by

$$\boldsymbol{\sigma} = \begin{bmatrix} \sigma_x \\ \sigma_y \\ \tau_{xy} \end{bmatrix}, \quad \boldsymbol{\tau} = \begin{bmatrix} \tau_{zx} \\ \tau_{yz} \end{bmatrix}, \quad \boldsymbol{\varepsilon} = \begin{bmatrix} \varepsilon_x \\ \varepsilon_y \\ \gamma_{xy} \end{bmatrix}, \quad \boldsymbol{\gamma} = \begin{bmatrix} \gamma_{zx} \\ \gamma_{yz} \end{bmatrix}, \quad \mathbf{E} = \begin{bmatrix} \mathrm{E_x} \\ \mathrm{E_y} \end{bmatrix}, \quad \mathbf{D} = \begin{bmatrix} \mathrm{D_x} \\ \mathrm{D_y} \end{bmatrix}, \tag{9}$$

E_z and D_z denote the transverse electric field and transverse electric displacement, respectively. p_z^1 and p_z^2 are normal tractions on the bottom and top surfaces, and ρ^k denotes the material mass density of the k th layer. Using the assumption $\sigma_z \simeq 0$, the linear constitutive equations relating the stresses $\boldsymbol{\sigma}, \boldsymbol{\tau}$ and electric displacements $\mathbf{D}$, D_z to the strains $\boldsymbol{\varepsilon}$, $\boldsymbol{\gamma}$ and electric field components $\mathbf{E}$, E_z are obtained as

$$\boldsymbol{\sigma} = \overline{\mathbf{Q}}\boldsymbol{\varepsilon} - \overline{\mathbf{e}}_3^{\mathrm{T}}\mathbf{E}_z, \quad \boldsymbol{\tau} = \hat{\mathbf{Q}}\boldsymbol{\gamma} - \hat{\mathbf{e}}\mathbf{E}, \quad \mathbf{D} = \hat{\mathbf{e}}^{\mathrm{T}}\boldsymbol{\gamma} + \hat{\boldsymbol{\eta}}\mathbf{E}, \quad \mathbf{D}_z = \overline{\mathbf{e}}_3\boldsymbol{\varepsilon} + \overline{\boldsymbol{\eta}}_{33}\mathbf{E}_z, \tag{10}$$

where $\overline{\mathbf{Q}}, \overline{\mathbf{e}}, \overline{\boldsymbol{\eta}}$ are the reduced elastic stiffnesses, piezoelectric stress constants and electric permittivities.

A quadrilateral plate element (Fig. 4) with four physical nodes and one electric node is used for the finite element discretization. Each physical node (node with physical coordinates) has seven mechanical DOF, namely, $u_{0_x}, u_{0_y}, w_0, w_{0,x}, w_{0,x}, \psi_{0_x}$, and ψ_{0_y}, and $n_\phi - 1$ electric DOF, ϕ_c^l. Thus, the electric potential variables ϕ_c^l can vary along x,y directions. To impose the equipotential condition over all elements covering an electroded segment, the surface potentials ϕ_j associated with the equipotential surface (or set of equipotential surfaces across the cross-section) are attached to an electric node p. The electric node does not have any physical coordinates and has n_ϕ DOF. This concept not only eliminates the need of imposing the equality constraints on the electric DOF for equipotential condition, but also results in significant reduction in the number of electric DOF.

As the highest derivatives of $u_{0_x}, u_{0_y}, \psi_{0_x}, \psi_{0_y}$ and ϕ_c^l appearing in the variational Eq. (8) are of first order, these are interpolated using C^0-continuous bilinear Lagrange interpolation functions. The presence of the second derivative of w_0 in the variational equation indicates that its interpolation function should have C^1 continuity at the element boundary, which is difficult to achieve for a quadrilateral element. This difficulty is circumvented by using the improved discrete Kirchhoff constraint approach [26]. In this approach, $w_{0,x}$ and $w_{0,y}$ are replaced by rotation variables θ_{0_x} and θ_{0_y}, which then require only C^0 continuity. w_0 and $\theta_{0_x}, \theta_{0_y}$ are interpolated independently, but the two are subsequently related by imposing the constraints $\theta_{0i} = w_{0,i}$ at discrete points on the element boundary as well as in the interior. The implementation enforces complete compatibility of the deflection field along the element sides [27]. For the purpose of computing consistent mass matrix and the load vector for the distributed transverse load, w_0 is interpolated assuming a bicubic function. The element mass matrix, element stiffness matrix and load vector for distributed transverse load are obtained from the variational Eq. (8).

At actuated surfaces (closed circuit condition), electric potentials have known prescribed values. At the sensory surfaces under open circuit condition, the electric loads are known (zero electric charge, i.e. $\int_{A_e} D_z\,\mathrm{d}x\,\mathrm{d}y = 0$, A_e being the area of electrode), but the electric potentials are unknown. The system vector U is partitioned into vectors of mechanical displacements $\overline{U}$, unknown voltages $\boldsymbol{\Phi}_s$ and known actuation voltages $\boldsymbol{\Phi}_a$. The equation of motion is accordingly partitioned and arranged as

$$\begin{bmatrix} \mathbf{M}^{uu} & \mathbf{0} & \mathbf{0} \\ \mathbf{0} & \mathbf{0} & \mathbf{0} \\ \mathbf{0} & \mathbf{0} & \mathbf{0} \end{bmatrix} \begin{Bmatrix} \ddot{\overline{\mathbf{U}}} \\ \ddot{\boldsymbol{\Phi}}_s \\ \ddot{\boldsymbol{\Phi}}_a \end{Bmatrix} + \begin{bmatrix} \mathbf{K}^{uu} & \mathbf{K}^{us} & \mathbf{K}^{ua} \\ \mathbf{K}^{su} & \mathbf{K}^{ss} & \mathbf{K}^{sa} \\ \mathbf{K}^{au} & \mathbf{K}^{as} & \mathbf{K}^{aa} \end{bmatrix} \begin{Bmatrix} \overline{\mathbf{U}} \\ \boldsymbol{\Phi}_s \\ \boldsymbol{\Phi}_a \end{Bmatrix} = \begin{Bmatrix} \overline{\mathbf{P}} \\ \mathbf{Q}_s \\ \mathbf{Q}_a \end{Bmatrix}. \tag{11}$$

When the actuator and sensor layers do not have any common electroded surface, $\mathbf{K}^{sa}$ is a null matrix. In case there is a common interface, the electric potential at the interface is considered as grounded. In both the cases, $\mathbf{K}^{sa}\boldsymbol{\Phi}_a = \mathbf{0}$. Also at the sensor surfaces, the applied electric charge is zero, $\mathbf{Q}_s = \mathbf{0}$. Considering these null matrices, Eq. (11) yields the output potentials as

$$\boldsymbol{\Phi}_s = -(\mathbf{K}^{ss})^{-1}K^{su}\overline{\mathbf{U}}. \tag{12}$$

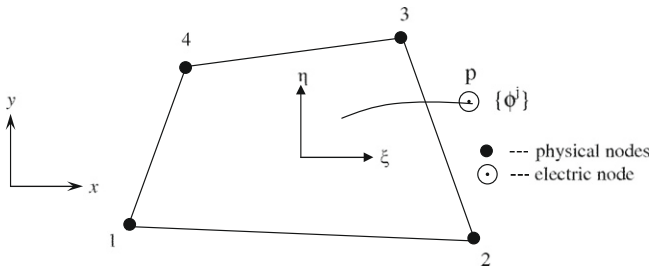

Fig. 4. The quadrilateral element with electric node.

Substituting Eq. (12) into Eq. (11) and introducing Rayleigh damping with damping matrix $\mathbf{C}^{uu}=\alpha_1\mathbf{M}^{uu}+\alpha_2\mathbf{K}^{uu}$ yields

$$\mathbf{M}^{uu}\ddot{\overline{\mathbf{U}}}+C^{uu}\dot{\overline{\mathbf{U}}}+\overline{\mathbf{K}}^{uu}\overline{\mathbf{U}}=\overline{\mathbf{P}}-\mathbf{K}^{ua}\mathbf{\Phi}_a, \tag{13}$$

where $\overline{\mathbf{K}}^{uu}=[\mathbf{K}^{uu}-\mathbf{K}^{us}(\mathbf{K}^{ss})^{-1}\mathbf{K}^{su}]$.

3. Active vibration control

3.1. Reduced order model in state space form

The finite element discretization requires a large number of DOF for accurate modeling. However, in numerical simulation of closed loop response using advanced control algorithms, a reduced order model is desired. Assuming that the lower modes, which are the most excitable ones due to lower associated energy, dominate the global response of the system, a truncated modal matrix $\boldsymbol{\psi}$ for the first m modes can be assumed to span the response vector $\overline{\mathbf{U}}$ as

$$\overline{\mathbf{U}}=\sum_{i=1}^{m}\boldsymbol{\psi}_i\hat{\eta}_i=\boldsymbol{\psi}\boldsymbol{\eta}, \tag{14}$$

where $\boldsymbol{\Psi}=[\boldsymbol{\Psi}_1\ \boldsymbol{\Psi}_2\ \cdots\ \boldsymbol{\Psi}_m]$ and $\boldsymbol{\eta}=[\hat{\eta}_1\ \hat{\eta}_2\ \cdots\ \hat{\eta}_m]^{\mathrm{T}}_{m\times 1}$ is the modal coordinates vector. Using transformation (14), the equation of motion (13) can be transformed to the reduced modal space as

$$\ddot{\boldsymbol{\eta}}(t)+\boldsymbol{\Lambda}\dot{\boldsymbol{\eta}}(t)+\boldsymbol{\Omega}\boldsymbol{\eta}(t)=\tilde{\mathbf{P}}(t)-\overline{\mathbf{K}}^{ua}\mathbf{\Phi}_a, \tag{15}$$

where $\boldsymbol{\Lambda}=\boldsymbol{\Psi}^{\mathrm{T}}\mathbf{C}^{uu}\boldsymbol{\Psi}$ and $\boldsymbol{\Omega}=\boldsymbol{\Psi}^{\mathrm{T}}\overline{\mathbf{K}}^{ua}\boldsymbol{\Psi}$ are diagonal matrices with generic terms $2\xi_i\omega_i$ and ω_i^2, respectively, where ξ_i is the modal damping ratio and ω_i is the undamped natural frequency of the i th mode, and

$$\tilde{\mathbf{P}}=\boldsymbol{\Psi}^{\mathrm{T}}\overline{\mathbf{P}},\quad \overline{\mathbf{K}}^{ua}=\boldsymbol{\Psi}^{\mathrm{T}}\mathbf{K}^{ua}. \tag{16}$$

Considering that all unknown potentials may not be measured, the sensor output vector $\mathbf{\Phi}_m$ is obtained as

$$\mathbf{\Phi}_m=\mathbf{C}_m\mathbf{\Phi}_s, \tag{17}$$

where $\mathbf{C}_m$ is the sensor location matrix given by $C_{ij}=\delta_{m_{ij}}$ for $i=1,\ \ldots,n_m$ where potentials at n_m number of sensors m_i are measured. The open-loop system represented by Eqs. (15), (12) and (17) can be represented in state space form, by introducing state variables $\mathbf{X}(t)=\mathrm{col}(\boldsymbol{\eta},\dot{\boldsymbol{\eta}})$, as

$$\dot{\mathbf{X}}(t)=\mathbf{A}\mathbf{X}(t)+\mathbf{B}_u\mathbf{u}_u(t)+\mathbf{B}_\phi\mathbf{u}_\phi(t),$$

$$\mathbf{Y}(t)=\mathbf{C}\mathbf{X}(t), \tag{18}$$

where $\mathbf{A}$ is the system state matrix, $\mathbf{B}_u$ and $\mathbf{B}_\phi$ are the mechanical and electrical input matrices, $\mathbf{C}$ is the output matrix, $\mathbf{u}_u(t)$ and $\mathbf{u}_\phi(t)$ are mechanical disturbances and electrical control input vectors, respectively, and $\mathbf{Y}(t)$ is the output vector, given by

$$\mathbf{A}=\begin{bmatrix}\mathbf{0} & \mathbf{I}\\ -\boldsymbol{\Omega} & -\boldsymbol{\Lambda}\end{bmatrix},\quad \mathbf{B}_u=\begin{bmatrix}\mathbf{0}\\ \boldsymbol{\Psi}^{\mathrm{T}}\end{bmatrix},\quad \mathbf{B}_\phi=\begin{bmatrix}\mathbf{0}\\ -\boldsymbol{\Psi}^{\mathrm{T}}\mathbf{K}^{ua}\end{bmatrix},\quad \mathbf{u}_u(t)=\overline{\mathbf{P}}(t),$$

$$\mathbf{C}=\begin{bmatrix}-\mathbf{C}_m[\mathbf{K}^{ss}]^{-1}\mathbf{K}^{su}\boldsymbol{\Psi} & \mathbf{0}\\ \mathbf{0} & -\delta_c\mathbf{C}_m[\mathbf{K}^{ss}]^{-1}\mathbf{K}^{su}\boldsymbol{\Psi}\end{bmatrix},\quad \mathbf{u}_\phi=\mathbf{\Phi}_a(t),\quad \mathbf{Y}(t)=\mathrm{col}(\mathbf{\Phi}_m,\delta_c\dot{\mathbf{\Phi}}_m), \tag{19}$$

where δ_c = 0 or 1 depending upon whether the time derivative of sensory voltage is measured or not.

3.2. Control algorithms

In CGVF control, the control input voltage is defined as

$$\mathbf{u}_\phi(t)=-\mathbf{G}\mathbf{Y}(t), \tag{20}$$

with $\mathbf{G}=[\mathbf{0}\ \mathbf{G}_v]$, where $\mathbf{G}_v$ is the velocity gain matrix. For a set of actuator–sensor pairs, it is a diagonal matrix. Substituting Eq. (20) into Eq. (18) yields

$$\dot{\mathbf{X}}(t)=(\mathbf{A}-\mathbf{B}_\phi\mathbf{G}\mathbf{C})\mathbf{X}(t)+\mathbf{B}_u\mathbf{u}_u(t),$$

$$\mathbf{B}_\phi\mathbf{G}\mathbf{C}=\begin{bmatrix}\mathbf{0} & \mathbf{0}\\ \mathbf{0} & \boldsymbol{\Lambda}_a\end{bmatrix}\quad \text{with } \boldsymbol{\Lambda}_a=\boldsymbol{\Psi}^{\mathrm{T}}\mathbf{K}^{ua}\mathbf{G}_v\mathbf{C}_m[\mathbf{K}^{ss}]^{-1}\mathbf{K}^{su}\boldsymbol{\Psi}. \tag{21}$$

It can be seen that the gain matrix $\mathbf{G}$ controls the closed-loop system through the modification of the damping (known as active damping) of the system and consequently the closed-loop poles. The piezoelectric coupling matrix, $\mathbf{K}^{au}$ and $\mathbf{K}^{su}$ for actuators and sensors, respectively, are generally not equal because of bending–stretching coupling of the actuators and

sensors. For a pair of actuator and sensor layers of the same thickness and symmetrically placed about the midplane, the membrane stiffnesses are equal but of opposite sign. In such cases, the active damping matrix $\mathbf{\Lambda}_a$ is not symmetric unlike the passive damping matrix $\mathbf{\Lambda}$ in Eq. (19), and it may cause instability in the closed-loop response. For truly collocated sensors and actuators, $\mathbf{\Lambda}_a$ is symmetric for which the velocity feedback is guaranteed to yield asymptotic stability of the response.

In LQR optimal control scheme [28], the control gain for a full state feedback is determined by minimizing a quadratic performance measure or cost function of the following form, which proportional to the system's vibration response measured through output $\mathbf{Y}(t)$ and to the control effort u_ϕ

$$J = \int_0^\infty [\mathbf{Y}^{\mathrm{T}}(t)\mathbf{Q}_Y\mathbf{Y}(t) + \mathbf{u}_\phi^{\mathrm{T}}(t)\mathbf{R}\mathbf{u}_\phi(t)]\,\mathrm{d}t. \tag{22}$$

$\mathbf{Q}_Y$ and $\mathbf{R}$ are the output and control input weighing matrices, which should be real symmetric positive definite. Larger elements in $\mathbf{Q}_y$ means higher priority on the vibration suppression ability, whereas larger values for elements of $\mathbf{R}$ means greater interest in reducing the control effort. For a steady state LQR controller, the optimal gain matrix $\mathbf{G}$ [Eq. (20)] is obtained as

$$\mathbf{G} = -[\mathbf{R}]^{-1}\mathbf{B}_\phi^{\mathrm{T}}\mathbf{P}, \tag{23}$$

where $\mathbf{P}$ is the solution of the steady state matrix Ricatti equation

$$\mathbf{A}^{\mathrm{T}}\mathbf{P} + \mathbf{P}\mathbf{A} - \mathbf{P}\mathbf{B}_\phi\mathbf{R}^{-1}\mathbf{B}_\phi^{\mathrm{T}}\mathbf{P} + \mathbf{C}^{\mathrm{T}}\mathbf{Q}_Y\mathbf{C} = \mathbf{0}. \tag{24}$$

Eq. (20) for control input demands the knowledge of the full state vector $\mathbf{X}$. If the output matrix $\mathbf{C}$ is square and non-singular, $\mathbf{X}$ can be readily obtained as $\mathbf{X}=\mathbf{C}^{-1}\mathbf{Y}$. However, if $\mathbf{X}$ cannot be directly obtained from $\mathbf{Y}$, it will be necessary to estimate the full state vector from the output vector. One such state estimator or observer is the Kalman–Bucy filter. It is optimal state observer for a system contaminated with measurement and plant (system) noise. In presence of a plant noise $\mathbf{u}_W$ and a measurement noise $\mathbf{u}_V$, the state Eq. (18) can be rewritten as

$$\dot{\mathbf{X}}(t) = \mathbf{A}\mathbf{X}(t) + \mathbf{B}_u\mathbf{u}_u(t) + \mathbf{B}_\phi\mathbf{u}_\phi(t) + \mathbf{B}_w\mathbf{u}_W(t),$$

$$\mathbf{Y}(t) = \mathbf{C}\mathbf{X}(t) + \mathbf{u}_V(t), \tag{25}$$

where $\mathbf{B}_w$ is the plant noise input matrix. The plant noise $\mathbf{u}_W$ can be regarded as including actuator noise and/or any external random disturbance. $\mathbf{u}_W$ and $\mathbf{u}_V$ are assumed to be uncorrelated white noise processes with positive definite intensities $\mathbf{W}(t)$ and $\mathbf{V}(t)$, respectively, so that the correlation matrices are given by

$$E[\mathbf{u}_W(t)\mathbf{u}_W^{\mathrm{T}}(t)] = \mathbf{W}\delta(t-\tau),$$

$$E[\mathbf{u}_V(t)\mathbf{u}_V^{\mathrm{T}}(t)] = \mathbf{V}\delta(t-\tau), \tag{26}$$

where E denotes the expectation operator. An estimate $\hat{\mathbf{X}}$ of the state vector $\mathbf{X}$ can be obtained by introducing in Eq. (18) an additional term of the form "gain multiplied by output error"

$$\dot{\hat{\mathbf{X}}}(t) = \mathbf{A}\hat{\mathbf{X}}(t) + \mathbf{B}_u\mathbf{u}_u(t) + \mathbf{B}_\phi\mathbf{u}_\phi(t) + \mathbf{L}[\mathbf{Y}(t) - \mathbf{C}\hat{\mathbf{X}}(t)], \tag{27}$$

where $\mathbf{L}$ is a $2m \times 2n_m$ observer gain matrix. The actual state $\mathbf{X}$ in the feedback control law given by Eq. (20) is now replaced by the estimated state $\hat{\mathbf{X}}$

$$\mathbf{u}_\phi(t) = -\mathbf{G}\hat{\mathbf{X}}(t). \tag{28}$$

An optimal solution $\mathbf{L}^*$ of the observer gain matrix $\mathbf{L}$ in Eq. (27) which minimizes the mean square value $E[\mathbf{e}^{\mathrm{T}}\,\mathbf{e}]$ of the steady state estimation error, $\mathbf{e} = \mathbf{X} - \hat{\mathbf{X}}$, is obtained as

$$\mathbf{L}^* = -\mathbf{M}\mathbf{C}^{\mathrm{T}}\mathbf{V}^{-1}, \tag{29}$$

where $\mathbf{M}$ is the covariance matrix of the steady state error $\mathbf{e}$ which is given by the solution of the following Riccati equation:

$$\mathbf{A}\mathbf{M} + \mathbf{M}\mathbf{A}^{\mathrm{T}} + \mathbf{B}_w\mathbf{W}\mathbf{B}_w^{\mathrm{T}} - \mathbf{M}\mathbf{C}^{\mathrm{T}}\mathbf{V}^{-1}\mathbf{C}\mathbf{M} = \mathbf{0}. \tag{30}$$

The combined closed-loop dynamic system with the controller and observer can be written using Eqs. (25) and (27)

$$\begin{bmatrix} \dot{\mathbf{X}} \\ \dot{\mathbf{e}} \end{bmatrix} = \begin{bmatrix} \mathbf{A} - \mathbf{B}_\phi\mathbf{G} & \mathbf{B}_\phi\mathbf{G} \\ \mathbf{0} & \mathbf{A} - \mathbf{L}^*\mathbf{C} \end{bmatrix} \begin{bmatrix} \mathbf{X} \\ \mathbf{e} \end{bmatrix} + \begin{bmatrix} \mathbf{B}_u \\ \mathbf{0} \end{bmatrix} \mathbf{u}_u + \begin{bmatrix} \mathbf{B}_w & \mathbf{0} \\ \mathbf{B}_w & -\mathbf{L}^* \end{bmatrix} \begin{bmatrix} \mathbf{u}_W \\ \mathbf{u}_V \end{bmatrix}. \tag{31}$$

This control philosophy combining LQR with steady state Kalman–Bucy filter is known as the linear quadratic Gaussian (LQG) control, based on the fact that the plant and measurement noise are Gaussian. The solution of Eqs. (24), (29)–(31) are obtained using MATLAB functions.

4. Numerical results

4.1. Validation

To validate the present formulation and the developed code, a cantilever hybrid composite plate ($0.2\,\mathrm{m}\times 0.2\,\mathrm{m}$) analyzed in the literature [13] is studied. The stacking sequence is mentioned from bottom to top. The plate consists of a four-layer angle–ply ($-45^\circ/45^\circ/-45^\circ/45^\circ$) T300/976 graphite–epoxy (Gr/Ep) composite substrate with two outer piezoelectric layers of PZT G1195N. The thickness of each composite layer is 0.25 mm and that of each piezoelectric layer is 0.1 mm. The material properties are listed Table 1. The plate is modeled with 15×15 elements, all attached to a single electric node ensuring equipotential condition of the top and bottom piezoelectric surfaces. The interfaces between the piezoelectric layers and the elastic substrate are grounded. For static analysis, the plate is subjected to a uniformly distributed load, $p_z^2 = -100\,\mathrm{N\,m^{-2}}$ and actuation voltages of equal magnitude applied to the top and bottom piezoelectric surfaces ($\phi^1=\phi^{n_\phi}=\phi_0$). The centreline deflection w (y=0.1 m, z=0) of the transversely loaded plate under actuation voltages $\phi_0=0$ and 50 V is plotted in Fig. 5 and compared with the results of Liu et al. [13], obtained using FSDT employing with the radial point interpolation method (RPIM). The two results agree very well. Next, the active vibration control of the cantilever plate vibrating due to initial disturbance of first mode is considered. The passive damping is taken as 0.8 percent for all modes. In this case, the top piezoelectric layer acts as an actuator and the bottom layer as a sensor. The reduced order model is obtained with first six modes. The closed-loop tip deflection, w(0.2, 0.1, 0), under CGVF control with different values of gain is plotted in Fig. 6, which compares well with the envelope of the response obtained by Liu et al. [13].

4.2. Control of hybrid composite plate

A rectangular ($0.2\,\mathrm{m}\times 0.05\,\mathrm{m}$) hybrid composite plate (a) made of four-layer T300/976 graphite–epoxy composite and two outer layers of monolithic PZT G1195N, as shown Fig. 7(a), is considered for further study. The cantilever plate is fixed at x=0, and free at the other three edges. It is modeled with a 24×8 regular mesh to obtain converged results for free vibration response. The top and bottom piezoelectric surfaces are treated as actuator and sensor, respectively, which are collocated in the conventional sense (Fig. 8(a)). In order to illustrate the effect of segmentation of electrodes on vibration control, the outer electroded surfaces of the piezoelectric layers are divided into one and sixteen segments (Fig. 9), respectively.

The first six closed-loop natural frequencies $f_i(=\omega_i/2\pi)$ and modal damping ratios of the hybrid composite plate (a) for CGVF control are presented in Table 2 for one and sixteen electrode segments of the actuator and sensor surfaces. The passive damping ratio is taken as 0.8 percent for all modes. The gain is taken as G=0.007 and 0.0015 for one and sixteen segments, respectively. It is observed that even for the low gains, the active modal damping ratio is negative for the third mode in case of one electrode segment and for the fifth mode in case of sixteen electrode segments. It means positive real part of the corresponding pole, causing instability in the closed-loop response for the conventionally collocated actuator/sensor pairs. The instability can be seen in the closed-loop transient responses of tip deflection, w(0.2, 0.025, 0) and control voltage presented in Fig. 10 for step excitation of 3 N and an impulse excitation of 0.01 N s applied at point A (Fig. 9) of the hybrid plate with one electrode segment. The responses are obtained using the truncated modal model with first six modes.

This instability is due to the fact that the active damping matrix $\mathbf{\Lambda}_a$ is not symmetric due to extension-bending coupling that makes the actuator/sensor pairs asymmetric in electromechanical sense. Such instability has been reported in the experimental studies by Akishita et al. [29] and Ghiringhelli and Zanardi [30] using conventionally collocated actuator/sensor pairs.

The instability in the closed-loop response in CGVF control can be remedied by using an electromechanically symmetric pairs of actuator and sensor, which is obtained by bonding two piezoelectric layers each to top and bottom of the elastic substrate, as shown in Fig. 8(b). A pair of symmetrically placed piezoelectric layers is then considered as the actuator/sensor. The gain is applied on the average of the measured values of potential derivative at the two sensors and the actuation voltage is applied evenly on the two actuators. This arrangement ensures a symmetric modal active damping matrix $\mathbf{\Lambda}_a$ and yields truly collocated actuator sensor-pairs. Table 3 shows the closed-loop modal damping ratios of the plate with the truly collocated actuator sensor arrangement, which are always positive for all modes for any value of gain, ensuring the stability of the closed-loop system. Fig. 11 presents the closed-loop responses for the tip-deflection and actuation voltage under step excitation, of the same plate with truly collocated actuator sensor pair with one electrode segment which too exhibit the stability of the system. Similar results for the 16 electrode case are presented in Fig. 12, showing the instability and stability of the conventionally and truly collocated actuator–sensor arrangements, respectively.

The effect of segmentation of electroded piezoelectric surfaces on natural frequencies and modal active damping ratios is illustrated in Table 3. It is observed that the active modal damping ratios for all flexural modes in the 16 electrode segment case are larger than those of the one-segment case for the same gain. Also, it is revealed from Figs. 11 and 12 that the same settling time (0.21 s) of the closed loop response is achieved in the 16-segment case at lesser gains (1.2 percent) than the one segment case (2 percent). These results show the effectiveness of segmentation of distributed actuators and

Table 1
Material properties.

Material	Y_1 (GPa)	Y_2 (GPa)	Y_3 (GPa)	G_{23} (GPa)	G_{13} (GPa)	G_{12} (GPa)	ν_{23}	ν_{13}	ν_{12}	ρ(kg m^{-3})
PZT-G1195N [31]	63.0	63.0	63.0	24.2	24.2	24.2	0.3	0.3	0.3	7600
T300/976 Gr/Ep [31]	150.0	9.0	9.0	2.5	7.1	7.1	0.3	0.3	0.3	1600
Gr/Ep [3]	132.5	10.8	10.8	3.4	5.7	5.7	0.24	0.24	0.24	1600
Al(A12024-T3) [3]	73	73	73	27.4	27.4	27.4	0.33	0.33	0.33	2710
	s_{11} ($\times 10^{-12}$m^{2}N^{-1})	s_{12} ($\times 10^{-12}$m^{2}N^{-1})	s_{13} ($\times 10^{-12}$m^{2}N^{-1})	s_{22} ($\times 10^{-12}$m^{2}N^{-1})	s_{23} ($\times 10^{-12}$m^{2}N^{-1})	s_{33} ($\times 10^{-12}$m^{2}N^{-1})	s_{44} ($\times 10^{-12}$m^{2}N^{-1})	s_{55} ($\times 10^{-12}$m^{2}N^{-1})	s_{66} ($\times 10^{-12}$m^{2}N^{-1})	
PZT-5H [22]	16.5	−4.78	−8.45	16.5	−8.45	20.7	43.5	43.5	42.6	7500
Matrix [22]	294	−88.2	−88.2	294	−88.2	294	764	764	764	1000
	d_{31} ($\times 10^{-12}$ mV^{-1})	d_{32} ($\times 10^{-12}$ mV^{-1})	d_{33} ($\times 10^{-12}$ mV^{-1})	d_{15} ($\times 10^{-12}$ mV^{-1})	d_{24} ($\times 10^{-12}$ mV^{-1})	$\varepsilon_{11}/\varepsilon_0$	$\varepsilon_{22}/\varepsilon_0$	$\varepsilon_{33}/\varepsilon_0$		
PZT-G1195N [31]	254.0	254.0	374.0	584.0	584.0	1728.8	1728.8	1694.9		
PZT-5H [22]	−274	−274	593	741	741	3130	3130	3400		
Matrix [22]						170	170	170		

Electrical permittivity of air, ε_0=8.85 $\times 10^{-12}$ Fm^{-1}.

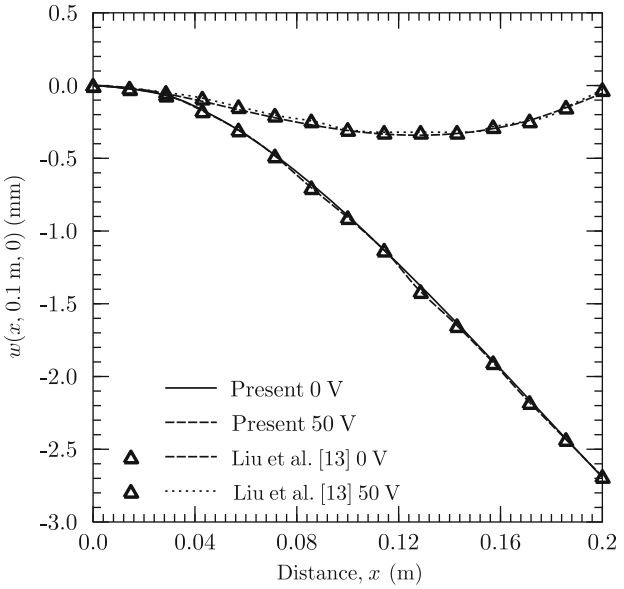

Fig. 5. The centerline deflection of cantilever hybrid angle–ply composite plate under uniform pressure loading and different actuation voltages.

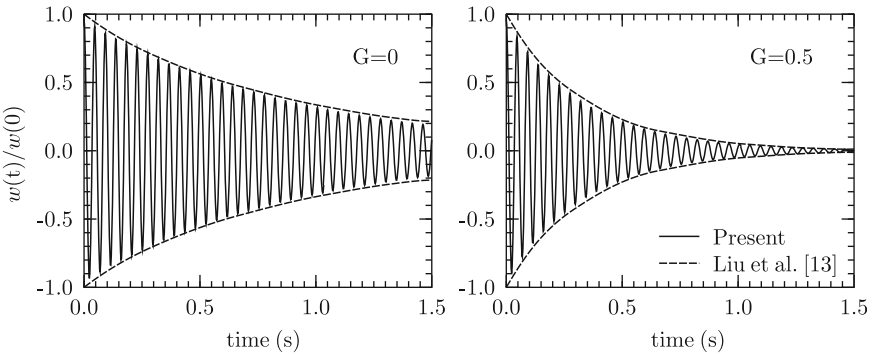

Fig. 6. The effect of velocity feedback control gain on the response of tip of cantilever hybrid angle–ply composite plate.

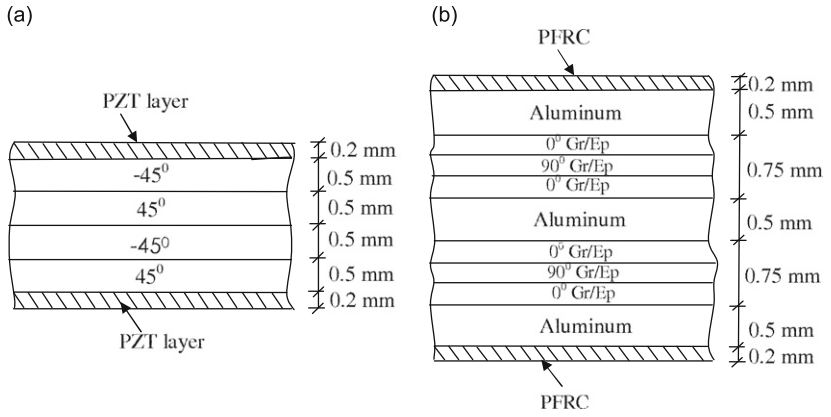

Fig. 7. Hybrid composite and FML plate configurations. (a) Hybrid composite plate. (b) Hybrid FML plate.

sensors in direct feedback control. The segmentation leads to a MIMO configuration. The peak voltage in the two actuator segments near the fixed edge (56.9 V) for the multi-segment electrode is higher than that of the one-segment case (36.8 V), but it is much smaller in the remaining actuator segments.

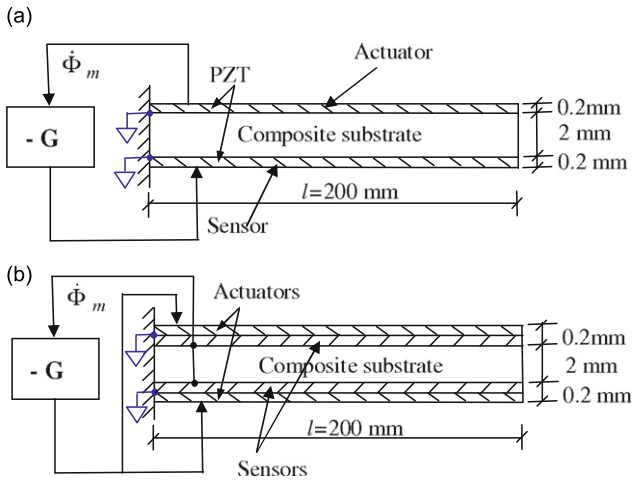

Fig. 8. Configurations of smart plates with (a) conventional and (b) truly collocated actuator and sensor layers.

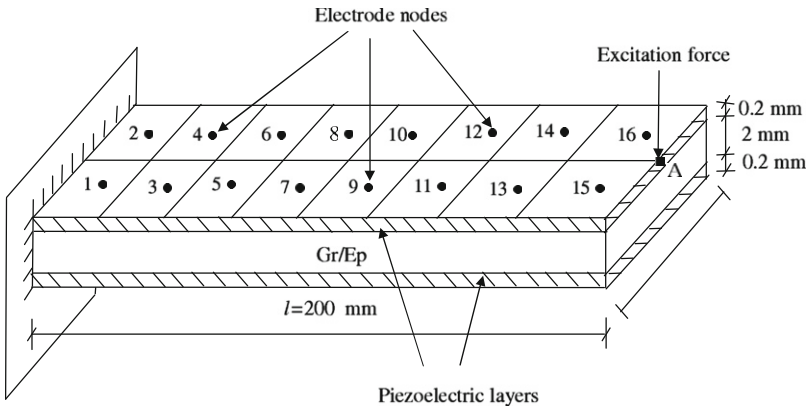

Fig. 9. Hybrid cantilever plate (a) with segmented electrodes.

Table 2
Closed-loop natural frequencies (f_i) and modal damping ratios (ξ_i) for plate (a) with conventionally collocated actuator/sensor under CGVF control.

Mode	One segment		Sixteen segments	
	f_i (Hz)	ξ_i (%)	f_i (Hz)	ξ_i (%)
1	40.9473	1.91	41.1600	1.20
2	253.661	1.79	256.280	2.01
3	412.082	−0.44	412.417	0.79
4	713.851	2.98	721.063	4.45
5	720.979	0.82	722.122	−0.32
6	1255.60	0.36	1257.54	1.26

The instability in the closed-loop response for direct feedback control due to asymmetric actuator sensor pairs is no longer an issue for optimal control laws. The effectiveness of LQR and LQG controllers is studied in this section for the cantilever hybrid plate (a) with single-segment and 16-segment electrodes for conventionally collocated actuator and sensor layers. The closed-loop natural frequencies and modal damping ratios for LQR control for both single- and multi-segment electrode cases are presented in Table 4 for first six modes with $\mathbf{Q}_y = 100\mathbf{I}$ and $\mathbf{R} = \mathbf{I}$. The damping is positive for all modes, establishing the stability of the system. The plate is excited by an impulse loading of 0.01 N s at point A. The open- and the closed-loop responses for the deflection and control voltage in LQR control for the single electrode case are plotted in Fig. 13 for different values of output weighing parameter ($\mathbf{Q}_y = Q_y\mathbf{I}$), while keeping the input weighing matrix constant as unity ($\mathbf{R} = \mathbf{I}$). As Q_y increases from 20 to 200, the settling time reduces from 0.53 to 0.17 s and the peak voltage increases from 19.0 to 72.0 V. The effect of sensor noise intensity $\mathbf{V}$ and plant noise intensity $\mathbf{W}$ on LQG control is illustrated in Fig. 14

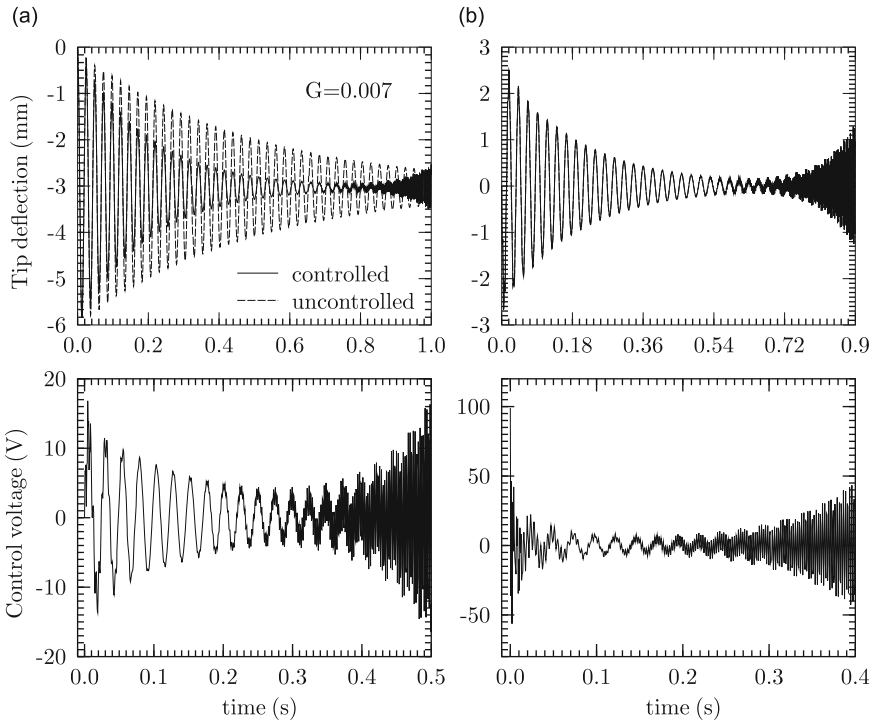

Fig. 10. Tip deflection and control voltage for CGVF control of plate (a) with one segment of conventionally collocated actuator/sensor. (a) Step excitation. (b) Impulse excitation.

Table 3
Closed-loop natural frequencies (f_i) and modal damping ratios (ξ_i) for plate (a) with truly collocated actuator/sensor under CGVF control.

Mode	One segment				Sixteen segments			
	Gain=0.01		Gain=0.03		Gain=0.01		Gain=0.03	
	f_i (Hz)	ξ_i (%)	f_i (Hz)	ξ_i (%)	f_i (Hz)	ξ_i (%)	f_i (Hz)	ξ_i (%)
1	40.9492	3.99	41.1267	10.40	41.2130	6.12	41.7381	16.70
2	253.961	3.65	256.449	9.38	264.465	16.26	312.594	25.19
3	412.159	0.80	412.159	0.80	412.883	3.18	416.828	7.84
4	712.543	7.13	702.593	20.03	705.037	52.62	722.270	0.81
5	720.924	0.81	720.915	0.80	722.281	0.81	2098.72	100
6	1255.41	0.80	1255.41	0.80	1257.72	10.38	1245.82	29.83

for the single-segment electrode, with Q_y=200 and **R**=**I**. As expected, increase in **V** has the same effect on response as the decrease in **W**. The two controllers LQR and LQG are compared in Fig. 15 for the plate with 16 electrode segments with $\mathbf{Q}_y$=100**I**, **R**=**I**, **V**=0.03 V^2 and **W**= 2.5×10^{-5}(N s)^2. The peak control voltage in actuator segments 1, 3, 5 and 7 is 241.0, 122.8, 163.1 and 122.5 V, respectively, for a settling time of 0.141 s in LQR control. For the same settling time, the corresponding peak voltages for LQG controller reduce to 137.4, 86.0, 69.7 and 62.7 V, respectively. A similar control effect can be obtained by actuating only six electrode segments (out of 16) near the fixed support, but with higher control voltages, which is illustrated in Fig. 15. Variations of response settling time and peak voltage with Q_y for single- and multi-segment cases are further compared in Fig. 16 for both LQR and LQG controllers. It confirms the superiority of multiple segmentation of actuators and sensors over the single-electrode case, yielding faster settling time for the same value of Q_y for both LQR and LQG controllers. This is possible due to higher active damping ratios in all modes in the multi-segment case for the same value of Q_y, as observed in Table 4.

4.3. Control of FML plate integrated with PFRC layers

A square hybrid plate (0.3 m × 0.3 m) made of FML of Al and Gr/Ep composite (Fig. 7(b)) and bonded to two outer PFRC layers is studied in this section. The PFRC is made of PZT-5H fibers and polymer matrix, whose properties are listed in

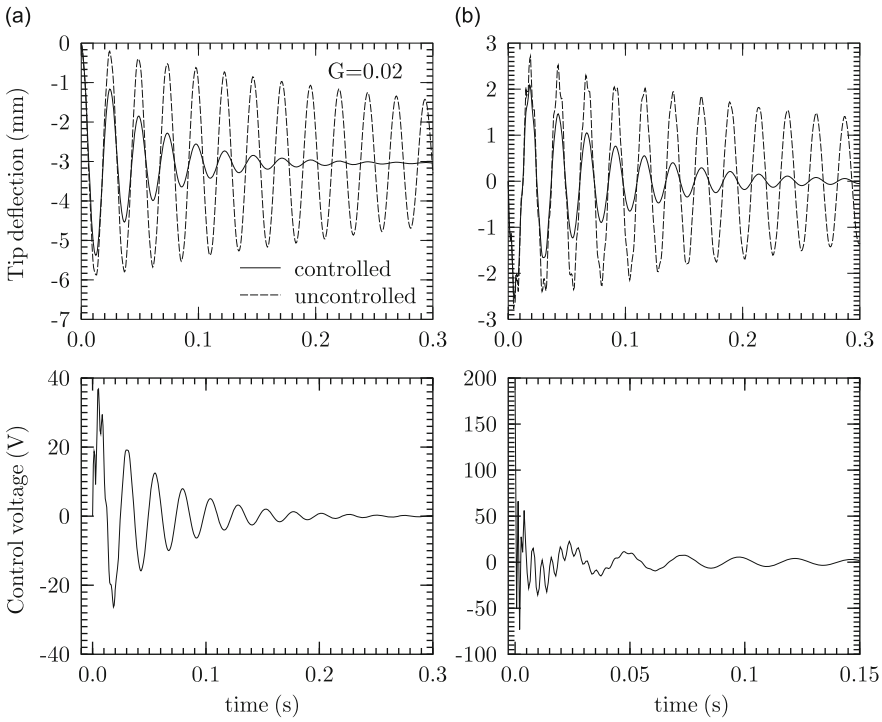

Fig. 11. Tip deflection and control voltage for CGVF control of plate (a) with one segment of truly collocated actuator/sensor under (a) step excitation (b) impulse excitations.

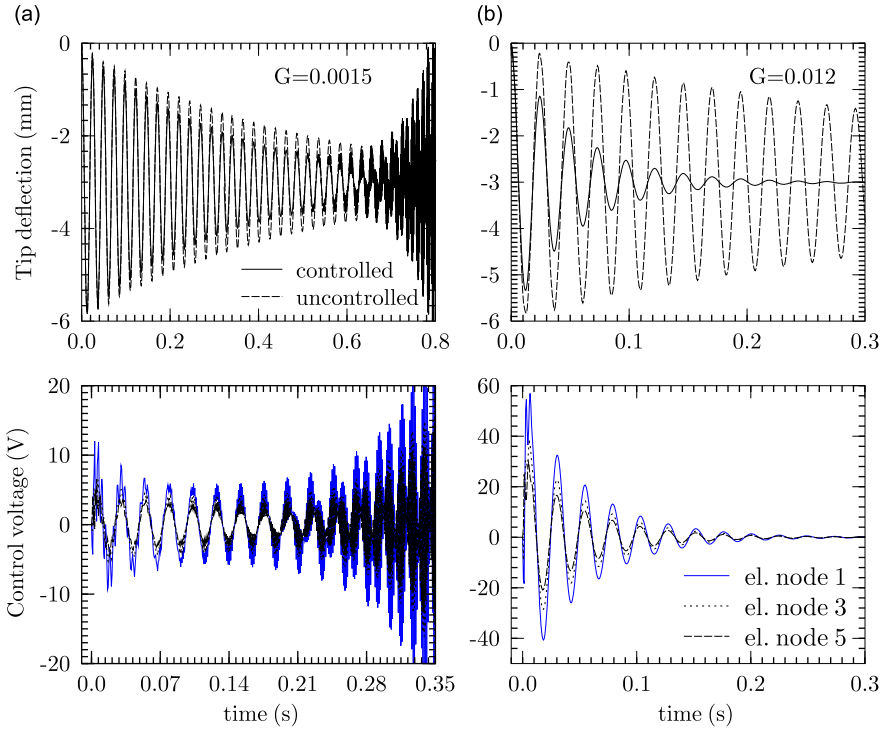

Fig. 12. Tip deflection and control voltage for CGVF control of plate (a) with 16 segments of conventionally and truly collocated actuator/sensor under step excitation. (a) Conventionally collocated. (b) Truly collocated.

Table 4
Closed-loop natural frequencies (f_i) and modal damping ratios ξ_i) for plate (a) under LQR control.

Mode	One segment		Sixteen segments	
	f_i (Hz)	ξ_i (%)	f_i (Hz)	ξ_i (%)
1	41.1428	6.17	41.6891	11.10
2	253.687	1.19	258.941	10.51
3	412.148	1.05	412.514	1.57
4	713.566	1.05	722.377	2.06
5	721.235	0.81	728.902	10.48
6	1255.43	0.80	1258.12	1.92

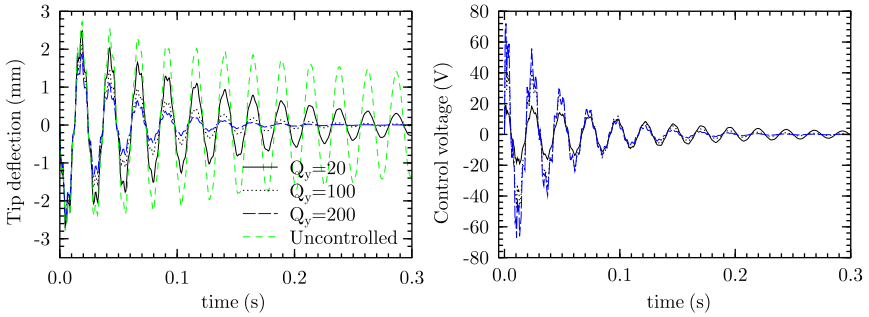

Fig. 13. Effect of Q_y on tip deflection and control voltage for LQR control of plate (a) under impulse excitation.

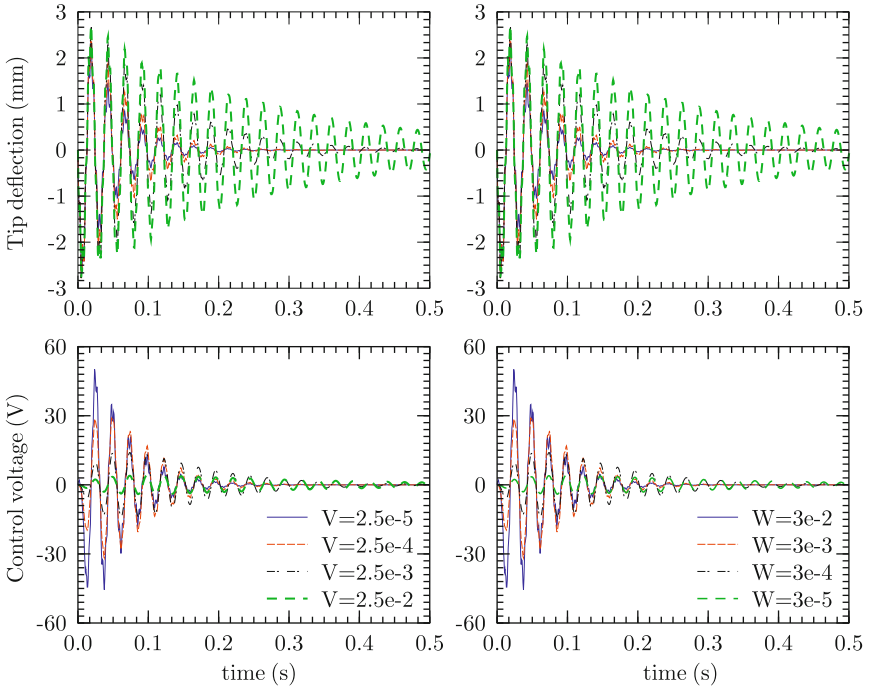

Fig. 14. Effect of noise intensities V and W on tip deflection and control voltage for LQG control of plate (a) under impulse excitation.

Table 1. The effective properties of the PFRC for a given fiber volume fraction v_f are computed using micromechanics model described in Section 2.1 The interfaces between the FML laminate and the PFRC layers are grounded. The bottom and the top electroded surfaces are considered as sensors and actuators, respectively. The plate is modeled with 400 (20×20) elements. Single-segment electrodes are considered at the PFRC surfaces which are modeled with one electric node. In the present model of the eleven-layer plate, the numbers of mechanical and electric DOF are 3087 ($21^2 \times 7$) and 886

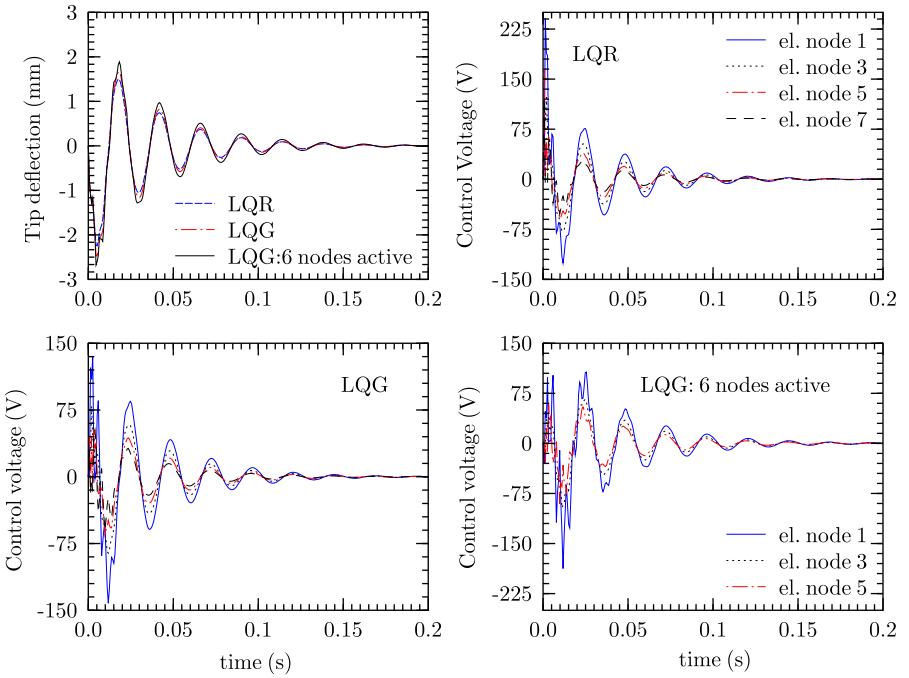

Fig. 15. Tip deflection and control voltage for optimal control of plate (a) with 16-segment electrode under impulse excitation.

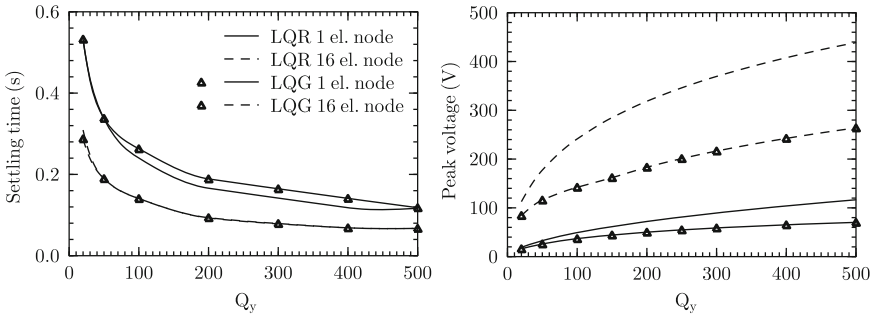

Fig. 16. Variation of settling and peak voltage with Q_y for plate (a).

$(21^2 \times 2+4)$, respectively. But, with the same mesh size, a coupled FE model based on the conventional LWTs (with constant w) would have 11025 $(21^2 \times (12 \times 2+1))$ mechanical DOF and 4410 $(21^2 \times 2 \times 5)$ electric (nodal) DOF, considering four sublayers for potential discretization. The one-fourth reduction in the number of DOF in the present model will cause one-sixteenth reduction in computation time, which is very significant for a dynamic/free vibration analysis. The difference will increase with the number of layers in the laminate. It establishes the computational efficiency of the present FE model.

The effects of fiber volume fraction v_f and fiber orientation α of the PFRC layers on the open loop natural frequencies ω_n are illustrated in Fig. 17 for a cantilever plate fixed at $x=0$. While the flexural frequencies ω_1 and ω_3 vary significantly with v_f and α, the second mode frequency ω_2 shows only marginal variation. Active vibration control response is obtained for a cantilever plate excited by a point load applied at point A and for an all-round simply supported plate excited by a load applied at the center. The LQG controller with $\mathbf{W}=0.003$ V^2, $\mathbf{V}=2.5\times10^{-5}$ N^2 s^2 and $\mathbf{R}=\mathbf{I}$ is employed for the optimal control. The closed-loop response for tip deflection w (0.3, 0.15, 0) of cantilever plate and central deflection w (0.15, 0.15, 0) of simply supported plate under impulse excitation, and the required control voltages are plotted in Fig. 18 for three values of piezo-fiber orientation ($\alpha=0^\circ, 45^\circ, 90^\circ$) for $Q_y=1000$. The cantilever plate is subjected to an impulse excitation of 0.06 N s and the simply supported plate to an excitation of 0.1 N s. The fiber volume fraction and dielectric ratio of PFRC layers are taken as $v_f=0.6$ and $\varepsilon_{33}^p/\varepsilon_{33}=20$. It is revealed that the participation of higher modes in the response decreases with α. Fig. 19 depicts the effect α on the response parameters, namely the peak deflection and the peak control voltage for a given settling time ($t_s=1$ s for cantilever plate and 0.1 s for simply supported plate). The response is obtained for a step excitation of 10 N for cantilever plate and 100 N for simply supported plate. The value of Q_y is adjusted to achieve the given settling time. For cantilever plate, PFRC with zero fiber angle is clearly the most efficient, and gives minimum peak deflection as well as control voltage. But the same does not hold well for the square simply supported plate, where the minimum peak

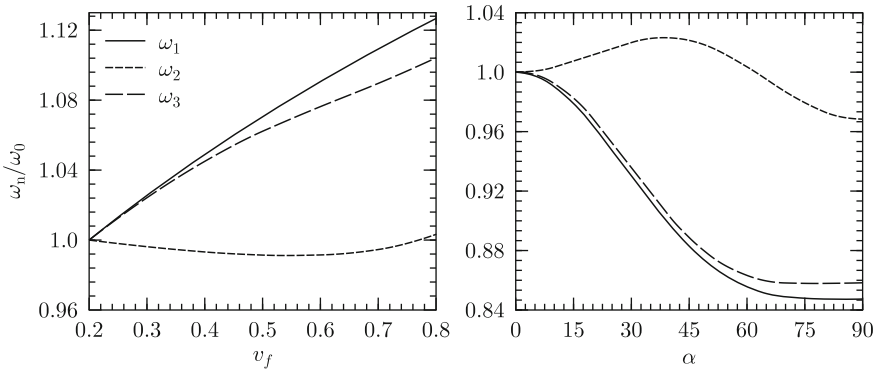

Fig. 17. Effect of fiber volume fraction and fiber orientation of PFRC on open-loop natural frequencies of cantilever hybrid FML plate (b).

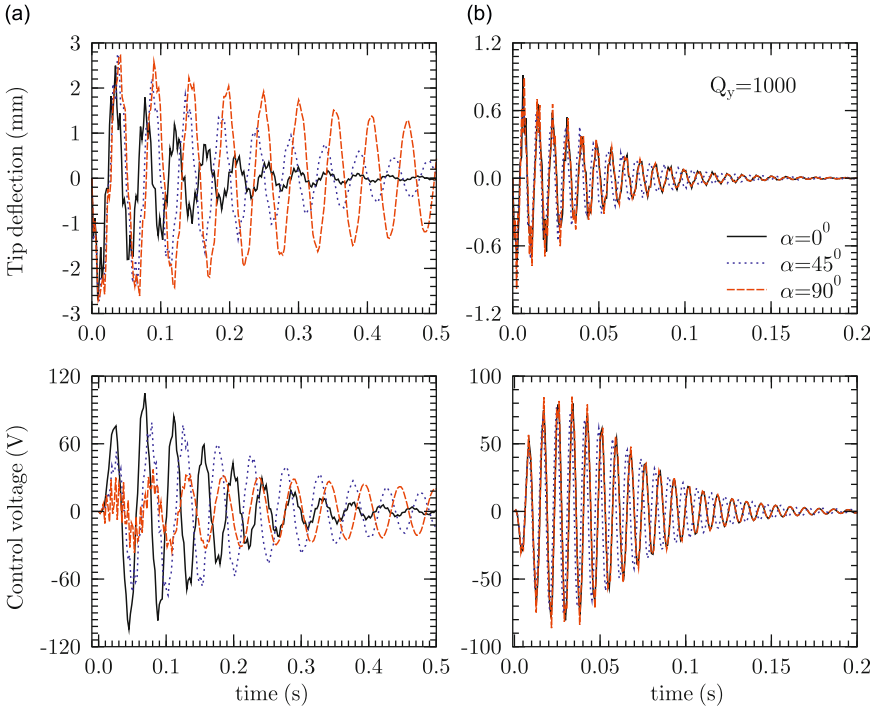

Fig. 18. Deflection and control voltage for FML plate (b) under impulse excitation for different fiber orientations. (a) Cantilever. (b) Simply supported.

deflection is achieved at $\alpha \approx 45^\circ$ and the minimum control voltage is achieved at $\alpha = 90^\circ$. Variations of the response parameters with v_f plotted in Fig. 20 reveal that both peak deflection and peak voltage for a given settling time reduce with v_f for both cantilever and simply supported boundary conditions. The ratio of dielectric constants ε_{33} of piezoelectric fiber and matrix ($\varepsilon^p_{33}/\varepsilon^m_{33}$) has significant effect on the control authority of the PFRC sensors and actuators. The variations of peak deflection and peak control voltage with the dielectric ratio are plotted in Fig. 21 for cantilever plate for $t_s = 1$ s. These plots reveal that the control authority of PFRC is significantly enhanced as $\varepsilon^p_{33}/\varepsilon^m_{33}$ reduces to unity and deteriorates with the increase in this ratio, as happens in commonly used materials. Equal dielectric constant ε_{33} of both the constituents in PFRC ensures uniform transverse electric field in both phases, resulting in high effective piezoelectric constants d^e_{ij}. Developments of matrix materials with ε^m_{33} of the order of ε^p_{33} would thus greatly enhance the performance of PFRC actuators and sensors.

5. Conclusions

The active vibration control of hybrid composite and FML plates integrated with monolithic piezoelectric and PFRC sensors and actuators is studied using an efficient and advanced layerwise plate theory. The theory is able to model the

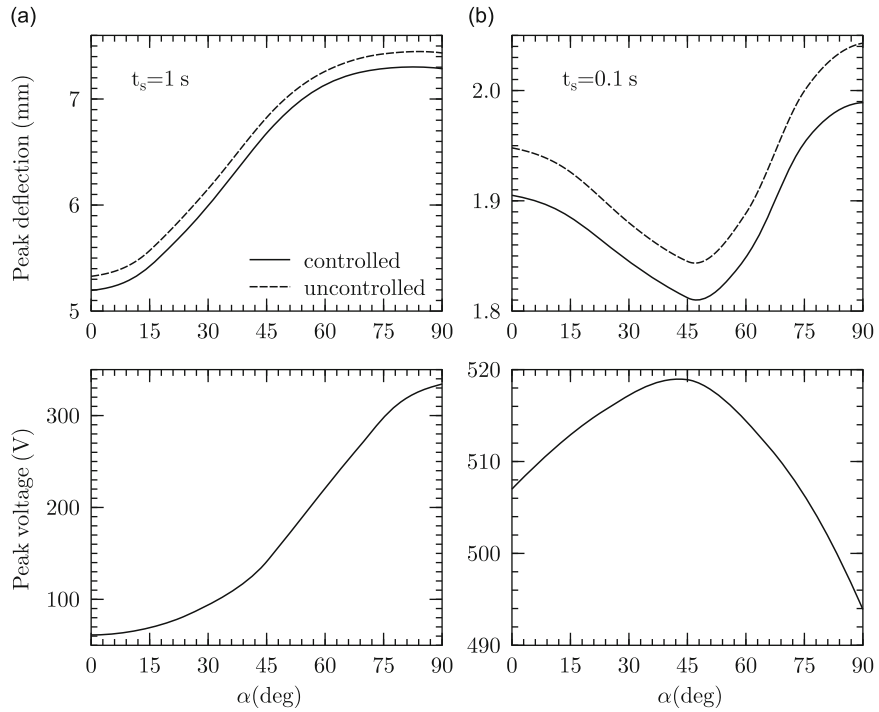

Fig. 19. Variation of peak deflection and peak voltage with PFRC fiber orientation for FML plate (b) under step excitation. (a) Cantilever. (b) Simply supported.

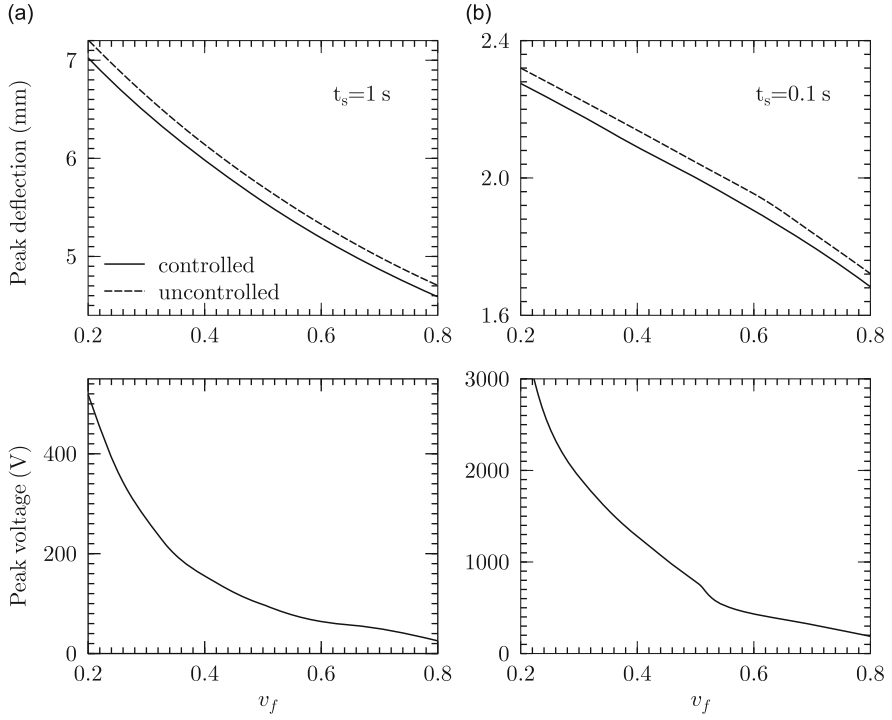

Fig. 20. Variation of peak deflection and peak voltage with PFRC fiber volume fraction for FML plate (b) under step excitation. (a) Cantilever. (b) Simply supported.

electromechanical inhomogeneities in the laminate configuration. The FE formulation models the equipotential condition of electrode segments accurately and at the same time reduces the number of electric DOF significantly using the novel concept of electric node. The numerical study reveals that:

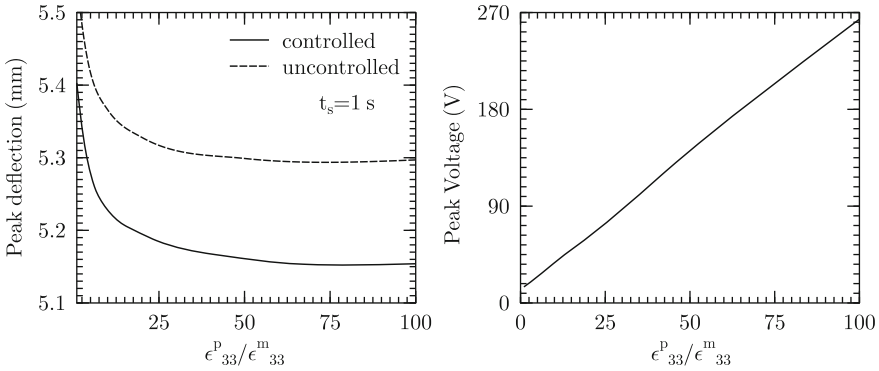

Fig. 21. Effect of dielectric ratio on the control response of cantilever hybrid FML plate (b) under step excitation.

(1) Piezoelectric sensors and actuators placed in conventional collocated sense cause instability in the closed-loop response of hybrid plates in direct feedback control. A truly collocated actuator–sensor arrangement to remove the instability is illustrated.
(2) Multiple segmentation of electrodes leads to faster attenuation of the closed-loop response for the same gain in direct feedback control and for the same output weighing parameters in optimal control.
(3) The peak control voltage to achieve the same settling time is smaller in LQG than LQR control for both single- and multi-segment electrodes.
(4) The fiber orientation of PFRC imparts directional actuation and sensing, which can be used efficiently to optimize the control performance of smart plates. The optimum fiber orientation depends on the boundary conditions and the optimization objective (minimize peak deflection or peak control voltage).
(5) Both peak deflection and peak control voltage can be reduced by increasing the volume fraction of piezoelectric fibers in PFRC.
(6) The effective piezoelectric constants and, therefore, the actuation/sensing authority of PFRC materials are maximum when the dielectric ratio is unity. Development of suitable matrix medium with dielectric constant ε^m_{33} of the order of ε^p_{33} would greatly enhance the performance of PFRC sensors and actuators.

References

[1] I. Chopra, Review of state of art of smart structures and integrated systems, *AIAA Journal* 40 (11) (2002) 2154–2187.
[2] K. Uchino, *Ferroelectric Devices*, Marcel Dekker Inc, New York, 2000.
[3] H.W. Nam, W. Hwang, K.S. Han, Stacking sequence design of fiber metal laminate for maximum strength, *Journal of Composite Materials* 35 (2001) 1654–1683.
[4] C.K. Lee, W.W. Chiang, T.C. O'Sullivan, Piezoelectric modal sensor/actuator pairs for critical active damping vibration control, *Journal of Acoustical Society of America* 90 (1) (1991) 374–384.
[5] T. Kim, J. Kim, Optimal distribution of an active layer for transient vibration control of a flexible plates, *Smart Materials and Structures* 14 (2005) 904–916.
[6] K. Umesh, R. Ganguli, Shape and vibration control of a smart composite plate with matrix cracks, *Smart Materials and Structures* 18 (2009) 1–13.
[7] S. Narayanan, V. Balamurugan, Finite element modelling of piezolaminated smart structures for active vibration control with distributed sensors and actuators, *Journal of Sound and Vibration* 262 (2003) 529–562.
[8] W. Hwang, H.C. Park, Finite element modeling of piezoelectric sensors and actuators, *AIAA Journal* 31 (5) (1993) 930–937.
[9] J.M.S. Moita, I.F.P. Correia, C.M.M. Soares, C.A.M. Soares, Active control of adaptive laminated structures with bonded piezoelectric sensors and actuators, *Computers and Structures* 82 (2004) 1349–1358.
[10] K.R. Kumar, S. Narayanan, The optimal location of piezoelectric actuators and sensors for vibration control of plates, *Smart Materials and Structures* 16 (2007) 2680–2691.
[11] G. Caruso, S. Galeani, L. Menini, Active vibration control of an elastic plate using multiple piezoelectric sensors and actuators, *Simulation Modelling Practice and Theory* 11 (2003) 403–419.
[12] J.X. Gao, Y.P. Shen, Active control of geometrically nonlinear transient vibration of composite plates with piezoelectric actuators, *Journal of Sound and Vibration* 264 (2003) 911–928.
[13] G.R. Liu, K.Y. Dai, K.M. Lim, Static and vibration control composite laminates integrated with piezoelectric sensors and actuators using radial point interpolation method, *Smart Materials and Structures* 13 (2004) 1438–1447.
[14] S. Raja, P.K. Sinha, G. Prathap, D. Dwarakanathan, Thermally induced vibration control of composite plates and shells with piezoelectric active damping, *Smart Materials and Structures* 13 (2004) 939–950.
[15] D.N. Kumar, S. Raja, T. Ikeda, Active vibration control of smart plates with partially debonded multilayered PZT actuators, *Smart Materials and Structures* 16 (2007) 1584–1594.
[16] B. Samanta, M.C. Ray, R. Bhatacharya, Finite element model for active control of intelligent structures, *AIAA Journal* 34 (9) (1996) 1885–1893.
[17] S.X. Xu, T.S. Koko, Finite element analysis and design of actively controlled piezoelectric smart structures, *Finite Elements in Analysis and Design* 40 (2004) 241–262.
[18] X.J. Dong, G. Meng, J.C. Peng, Vibration control of piezoelectric smart structures based on system identification technique: numerical simulation and experimental study, *Journal of Sound and Vibration* 297 (2006) 680–693.
[19] Z.K. Kusculuoglu, T.J. Royston, Finite element formulation for composite plates with piezoceramic layers for optimal vibration control applications, *Smart Materials and Structures* 14 (2005) 1139–1153.

[20] S. Kapuria, S.D. Kulkarni, An efficient quadrilateral element based on improved zigzag theory for dynamic analysis of hybrid plates with electroded piezoelectric actuators and sensors, *Journal of Sound and Vibration* 315 (2008) 118–145.
[21] A.A. Bent, Piezoelectric Fiber Composites for Structural Actuation, MS Thesis, Massachusetts Institute of Technology, USA, 1994.
[22] A.A. Bent, N.W. Hagood, J.P. Rodgers, Anisotropic actuation with piezoelectric fiber composites, *Journal of Intelligent Material Systems and Structures* 6 (1995) 338–349.
[23] S. Kapuria, P. Kumari, Three dimensional piezoelasticity solution for dynamic response of cross-ply cylindrical shells with piezoelectric fiber reinforced composite actuators and sensors, *Journal of Composite Structures* (2009),in press, doi:10.1016/j.compstruct.2010.02.016.
[24] S. Kapuria, S.D. Kulkarni, Static electromechanics response of smart composite/sandwich plates using an efficient finite element with physical and electric nodes, *International Journal of Mechanical Sciences* 51 (2009) 1–20.
[25] H.F. Tiersten, *Linear Piezoelectric Plate Vibrations*, Plenum Publishing Corporation, New York, 1969.
[26] C. Jeychandrabose, J. Kirkhope, L. Meekisho, An improved discrete Kirchhoff quadrilateral thin-plate bending element, *International Journal for Numerical Methods in Engineering* 24 (1987) 635–654.
[27] O.C. Zienkiewicz, R.L. Taylor, *The Finite Element Method, Vol. 2: Solid Mechanics*, Butterworth–Heinemann, Oxford, 2000.
[28] L. Meirovitch, *Dynamics and Control of Structures*, John Wiley and Sons, Dordrecht, 1989.
[29] S. Akishita, Y.I. Mitani, H. Miyaguchi, Sound transmission control through rectangular plate by using piezoelectric ceramics as actuators and sensors, *Journal of Intelligent Material Systems and Structures* 5 (1994) 371–378.
[30] G.L. Ghiringhelli, M. Zanardi, Evaluation of piezoelectric active control systems for vibration suppression, in: *Computational Methods for Smart Structures and Materials*, WIT Press, Boston, 1998.
[31] J. Jiang, R.C. Batra, Effect of electromechanical coupling on static deformations and natural frequencies, *IEEE Transactions on Ultrasonic, Ferroelectric, and Frequency Control* 52 (2005) 1079–1093.